Solar Physics (2006) 235: 345–368
DOI: 10.1007/s11207-006-0100-y

EVOLUTION OF CORONAL MASS EJECTIONS IN THE INNER HELIOSPHERE: A STUDY USING WHITE-LIGHT AND SCINTILLATION IMAGES

P. K. MANOHARAN
Radio Astronomy Centre, Tata Institute of Fundamental Research, P.O. Box 8, Udhagamandalam (Ooty) 643001, India
(e-mail: mano@ncra.tifr.res.in)

(Received 22 October 2005; accepted 2 February 2006)

Abstract. Knowledge of the radial evolution of the coronal mass ejection (CME) is important for the understanding of its arrival at the near-Earth space and of its interaction with the disturbed/ambient solar wind in the course of its travel to 1 AU and further. In this paper, the radial evolution of 30 large CMEs (angular width $>150^\circ$, i.e., halo and partial halo CMEs) has been investigated between the Sun and the Earth using (i) the white-light images of the near-Sun region from the *Large Angle Spectroscopic Coronagraph* (LASCO) onboard SOHO mission and (ii) the *interplanetary scintillation* (IPS) images of the inner heliosphere obtained from the Ooty Radio Telescope (ORT). In the LASCO field of view at heliocentric distances $R \leq 30$ solar radii ($R_\odot$), these CMEs cover an order of magnitude range of initial speeds, $V_{\rm CME} \approx 260$–2600 km s^{-1}. Following results have been obtained from the speed evolution of these CMEs in the Sun–Earth distance range: (1) the speed profile of the CME shows dependence on its initial speed; (2) the propagation of the CME goes through continuous changes, which depend on the interaction of the CME with the surrounding solar wind encountered on the way; (3) the radial-speed profiles obtained by combining the LASCO and IPS images yield the factual view of the propagation of CMEs in the inner heliosphere and transit times and speeds at 1 AU computed from these profiles are in good agreement with the actual measurements; (4) the mean travel time curve for different initial speeds and the shape of the radial-speed profiles suggest that up to a distance of $\sim 80\ R_\odot$, the internal energy of the CME (or the expansion of the CME) dominates and however, at larger distances, the CME's interaction with the solar wind controls the propagation; (5) most of the CMEs tend to attain the speed of the ambient flow at 1 AU or further out of the Earth's orbit. The results of this study are useful to quantify the drag force imposed on a CME by the interaction with the ambient solar wind and it is essential in modeling the CME propagation. This study also has a great importance in understanding the prediction of CME-associated space weather at the near-Earth environment.

1. Introduction

Coronal mass ejections (CMEs) are the most energetic and the largest phenomena associated with the eruption of plasma and magnetic field from the Sun. The Earth-directed CMEs are the major cause for the severe geo-magnetic storms (*e.g.*, Gosling *et al.*, 1991). Primary factors determining the geoeffectiveness are the direction of propagation of the CME, its speed, size, density, and orientation and strength of the magnetic field at the near-Earth space. Before the advent of the regular white-light

imagery of CMEs by the SOHO spacecraft, numerous early studies attempted (1) to understand the dynamics of the large-scale structure of CME-associated disturbances in the Sun–Earth space, and (2) to find the relationship between the speed and transit time of such disturbances (see reviews by Dryer, 1974, 1994; Gary *et al.*, 1984; Gosling, 1990; Hildner, 1977; MacQueen, 1980; Stewart, 1980). For example, several workers combined the near-Sun coronal shock measurements, mainly from the metric type II radio bursts, with observations from other techniques such as (i) Doppler scintillation measurements, (ii) the detection of interplanetary shock by one or more space missions, (iii) cosmic ray measurements (*i.e.*, 'Forbush decrease'), (iv) cometary fading, and (v) shock sudden commencements (SSCs) at the Earth (*e.g.*, Woo *et al.*, 1985; Lyubimov, 1968; Pinter, 1973; Dryer *et al.*, 1974) and derived the radial evolution of speed for a number of disturbances represented by the power-law form, $V \sim R^{-\alpha}$. The interplanetary scintillation (IPS) measurements at 102 MHz also provided the similar power-law profiles for the deceleration of the shocks and the index, α, varied from one event to the other in the range, $0.25 < \alpha < 1$ (Vlasov, 1992). However, in these studies, in general, the initial speed of the CME was estimated from the linear extrapolation with the coronal shock speed as computed from the drift rate of metric type II radio bursts.

The early work which addressed the large-scale structure of the propagating transients was based on IPS measurements of a large number of radio sources from the Cambridge IPS array operating at 81.5 MHz (*e.g.*, Hewish, Tappin, and Gapper, 1985; Purvis *et al.*, 1987). At this observing frequency, the detection of excessive scintillation generated by the solar wind transient is more pronounced at heliocentric distances, $R > 0.7$ AU because at about 0.5–0.6 AU the weak to strong scintillation transition occurs (1 AU $= 1.496 \times 10^8$ km; 1 solar radius, $R_\odot = 6.96 \times 10^5$ km; 1 AU $= 214.94\ R_\odot$). At distances within the transition region, the scintillation becomes saturated (Gapper *et al.*, 1982; Manoharan, 1993; also refer to Section 3 and discussions on Figure 2). The Cambridge IPS imaging has detected a large number of disturbances associated with co-rotating interaction regions, which are caused by the high-speed solar wind originating above the coronal hole regions on the Sun (*e.g.*, Hewish, Tappin, and Gapper, 1985). Tappin *et al.* (1988) and Odstrcil (2003) compared the observed scintillation images with the pattern obtained from the three-dimensional magnetohydrodynamic (MHD) simulated models and also demonstrated the effect of line of sight integration on the IPS sky-plane images for both halo and partial halo CMEs. However, in the recent years, IPS measurements at high observing frequency (similar to the measurements report in this paper, at 327 MHz, and sensitive to the detection of CME-associated disturbances at distances outside 50 $R_\odot$) on a large number of radio sources and Doppler scintillation data have provided CMEs' size, speed, turbulence level, and mass and their evolutions at range of distances from the Sun (*e.g.*, Manoharan *et al.*, 1995, 2000, 2001; Janardhan *et al.*, 1996; Tokumaru *et al.*, 2003; Woo *et al.*, 1995).

A large number of multi-dimensional, time-dependent MHD models have also been simulated to understand the interplanetary evolution of disturbances generated

by solar events (Han, Wu, and Dryer, 1988; for a review and some results, refer to Dryer, 1994). In these models, the crucial parameters were (i) coronal shock speed, which was extrapolated from the drift rate of metric type II radio bursts, and (ii) piston driving duration (*e.g.*, the duration of the X-ray flare was taken as a proxy for the piston duration). Moreover, these models did not consider the evolution of disturbance at distances between the Sun and 18 $R_{\odot}$. These models have been extensively used to understand the predictive capabilities of interplanetary disturbances in the Sun–Earth connection and the speed–deceleration profiles, *i.e.*, power-law form, revealed by them were nicely matching with the experimental results (see Smith and Dryer, 1990). Another important point is that the earlier experimental (see review by Anzer, 1980) as well as the numerical simulation studies (*e.g.*, Smith and Dryer, 1990; Odstrcil, 2003) emphasized the importance of considering the background solar wind in the study of evolution of interplanetary disturbances in the distance between the Sun and Earth. For example, based on the aforementioned numerical code (Han, Wu, and Dryer, 1988), some of the simulated MHD models made have been extremely useful to understand the interactions among magnetic cloud, background solar wind, and propagating shock and results indicated the compression and deflection of magnetic cloud against the radial direction of the solar wind (*e.g.*, Cargill *et al.*, 1996; Vandas *et al.*, 1996). Therefore, the interaction of the CME with the background solar wind is likely to play a crucial role in determining the impact of the CME (*i.e.*, the intensity of the storm) at the Earth's magnetosphere.

In the aforementioned simulated models and some of the experimental studies, the main disadvantage was the assumption of initial conditions of the CME extrapolated from the proxy metric type II radio bursts. Because type II bursts occur in solar events, examples flares and CMEs, they often do not generate interplanetary type II bursts or shocks (Cane and Reames, 1988; Gopalswamy *et al.*, 1998). Further, CMEs have been observed with/without coronal shocks. However, there seems to be an excellent association of interplanetary shocks with fast CMEs (Sheeley *et al.*, 1985; Cane, Sheeley, and Howard, 1987; Gopalswamy *et al.*, 2005). Moreover, long-lived solar energetic particle events are also well associated with fast CMEs indicating particle acceleration by the shocks driven by CMEs (*e.g.*, Reames, 1996). Therefore, a better understanding of associations (as well as correlations) is essential among the following near-Sun and the interplanetary manifestations: coronal shock, X-ray duration, initial speed and size of the CME, extension of the shock into the interplanetary space, and arrival times, speeds, and magnetic field intensities of shock and interplanetary CME at the Earth's orbit or elsewhere. This paper focuses on the study of evolution of speed profiles of a set of fast, wide CMEs by detecting their onset times at increasing heliocentric distances with the help of white-light and IPS images.

In the recent years, several authors have investigated the CME speeds at the near-Sun region, mainly from the space-borne white-light images and their implications at about 1 AU (*e.g.*, Lindsay *et al.*, 1999; Gopalswamy *et al.*, 2000; Webb *et al.*,

2000; Srivastava and Venkatakrishnan, 2002; Cane and Richardson, 2003; Vilmer *et al.*, 2003; Zhang *et al.*, 2003; Manoharan *et al.*, 2004). In particular, the effective acceleration of the CME derived from the speeds near the Sun and at 1 AU has been employed to predict the travel time of the CME to 1 AU (*e.g.*, Gopalswamy *et al.*, 2001; Sun *et al.*, 2003; Manoharan *et al.*, 2004). However, as discussed previously, since the solar wind is made up of steady and turbulent flows, discontinuities, and shocks and also CME tends to locally adopt to the ambient solar wind (*e.g.*, Gosling and Riley, 1996; Gopalswamy *et al.*, 2000), these are likely to contribute a significant change on the propagation of the CME. The recent study by Manoharan *et al.* (2004) has also emphasized the importance of the interaction between the CME and the ambient solar wind as well as the CME–CME interaction during the propagation of the CME.

In order to explain the evolution of a CME, the essential requirement therefore is the completeness of observations at several points on the Sun–Earth (or 1-AU) path. In this paper, the near-Sun images from the *Large Angle Spectroscopic Coronagraph* (LASCO) onboard SOHO mission (Brueckner *et al.*, 1995) and the inner heliosphere images provided by the *IPS* measurements from the Ooty Radio Telescope (ORT) at 327 MHz (Manoharan *et al.*, 2000, 2001) are employed to study the realistic evolution of the CME that occurs in the solar wind. The LASCO measurements and other available supportive data have been cataloged by Yashiro and his coworkers (refer to Yashiro *et al.*, 2004; also visit to *http://cdaw.gsfc.nasa.gov/CME_list*). At the ORT (for description of the telescope system refer to Swarup *et al.*, 1971; Selvanayagam *et al.*, 1993), the regular monitoring of IPS on a grid of large number of compact radio sources ($\sim$700 galaxies/quasars per day) provides the images of CMEs as well as the ambient solar wind plasma and reliable estimates of their speeds and associated levels of density turbulence at all heliographic latitudes and at a range of distances from the Sun to 1 AU.

This study reports the analysis of the radial evolution of 30 large CMEs, of which 23 events are full halo CMEs and the remaining are partial halos. Since the angular widths of these partial-halo CMEs are also large ($>150^\circ$), when viewed radially along the direction of propagation, they would also appear as halo CMEs. In other words, particularly the direction of propagation of the CME away from the Sun–Earth-directed line and the projection of the white-light image on the plane of sky give a partial halo view. These partial halos, in other physical aspects like mass, energy, and speed, should be similar to typical full halos. Events for the present study have been selected based on the following criteria: (1) the availability of both white-light measurements and IPS data to cover the Sun to 1 AU distance; and (2) for each event, the detection of its corresponding interplanetary shock (IP shock) and/or interplanetary CME (ICME, *i.e.*, ejecta, EJ, and/or magnetic cloud, MC) near the Earth's orbit. The next section describes the near-Sun images of CME obtained from LASCO, the method of estimation of the initial speed, and the arrival of CME at 1 AU. The IPS images of CME are described in Section 3. The analysis of 'speed-distance' profile, transit time and speed of CME at the Earth's orbit, and

internal energy of CME are discussed in Section 4. The results are summarized in Section 5.

2. LASCO Images and CME Initial Speed

The field of view of LASCO coronagraphs extends up to a heliocentric radius of $R \approx 30\,R_\odot$ and the white-light images of this field of view are recorded at regular time interval. The 'height-time' plot of a CME is drawn by identifying the leading edge of the CME on the sequence of white-light images. Figure 1 shows the examples of LASCO white-light images in the sky plane and the 'height–time' plot of a halo CME observed in association with an X5.7 flare on July 14, 2000.

A straight-line fit to the 'height–time' data yields the linear speed and the second-order fit provides the radial-speed profile, $V_{\rm CME}(R)$, and an effective acceleration of the CME. In the LASCO field of view, events under consideration fall in one of these categories of speed profiles, $V_{\rm CME}(R)$: (1) steadily moving CMEs (*i.e.*, constant speed events), (2) accelerating CMEs, and (3) decelerating cases. However, in the present study, the linear speed derived from the height–time plot is considered as

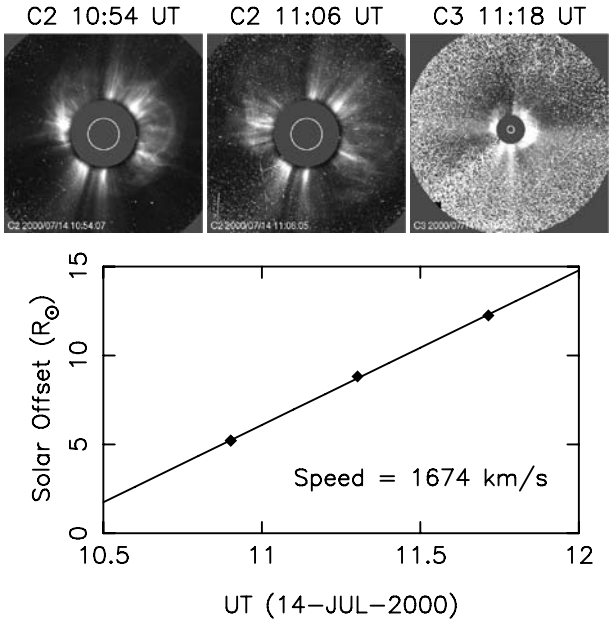

Figure 1. Examples of white-light images of the halo CME observed on July 14, 2000, in association with X5.7 solar flare. These images are from LASCO/SOHO C2 and C3 coronagraphs, which cover radial distances $6\,R_\odot$ and $32\,R_\odot$, respectively. In each image, the *inner circle* represents the solar disk. The 'height–time' plot (*bottom panel*) has been derived by measuring the leading edge of the white-light images in the plane of sky.

the initial speed of the CME, V_{CME}. Speeds of these 30 events cover a wide range of ~260–2600 km s^{-1}. The average initial speed, $\langle V_{\mathrm{CME}} \rangle = 1091$ km s^{-1}, indicates that most of the CMEs are high-speed events.

2.1. Interacting events

For each CME, the location of the associated flare and/or filament activities on the Sun has been identified with the help of EIT and LASCO images and the flare list provided by the NOAA (available at *ftp://ftp.ngdc.noaa.gov*). Most of the events, 21 out of 30 CMEs, originated close to the center of the disk, *i.e.*, within 35° of longitude and latitude from the center of the photosphere. Since the phenomenon of interaction between CMEs in the interplanetary medium may cause change in the trajectory of the CME and/or lead to the merger (*e.g.*, Gopalswamy *et al.*, 2002; Manoharan *et al.*, 2004), in the present study, the interacting cases have also been identified by considering (1) nearly same originating locations on the Sun, and (2) the difference between the starting times of CMEs within a day. The EIT and LASCO images have been examined to identify the interaction of CME(s). In addition, the list of CMEs analyzed by Gopalswamy *et al.* (2001, 2002) and Manoharan *et al.* (2004) have been also used to identify the interacting cases.

2.2. CME arrival at 1 AU

The arrival of IP shock associated with each CME at 1 AU has been determined by the careful examination of interplanetary magnetic field data and solar wind plasma density, speed, and temperature measurements obtained from the *Wind* spacecraft (MFI and SWE instruments) or ACE spacecraft (MAG and SWEPAM instruments). The onset of the interplanetary CME (*i.e.*, ejecta, EJ, and/or magnetic cloud, MC) at 1 AU followed after the IP shock has also been identified with the data sets mentioned previously by identifying one or more of the following characteristics: (1) strong magnetic field, (2) smooth rotation of direction of the magnetic field, (3) low proton temperature, (4) high charge state, and (5) counter-streaming electrons (*e.g.*, Lepping *et al.*, 1997; Neugebauer and Goldstein, 1997). However, the presence of these signatures singly or together and their magnitudes varied from one CME to the other and a few cases are likely to have uncertainties of about an hour or so in arrival times.

In Table I, observations and results of 30 CMEs under study are given in the following order: LASCO CME date, time, initial speed, CME type (halo, H, or partial halo, PH), associated flare/filament eruption location and class, interplanetary shock arrival date and time at 1 AU, EJ/MC arrival date, time, speed at 1 AU, and observed CME travel time to 1 AU. The last three columns of the table show the parameters estimated with the help of IPS measurements at distances $R > 50\,R_{\odot}$ as described in the following section.

TABLE I

List of white-light CMEs, IP shocks, ICMEs, and IPS data.

	CME				Flare		1-AU IP shock		1-AU ICME (MC/EJ)				IPS fitted		
No.	Date	h:m	V_{CME} (km s^{-1})	H/P	Class	Location	Date	h:m	Date	h:m	V_{ICME} (km s^{-1})	TT (h)	α	$V_{1\,AU}$ (km s^{-1})	TT (h)
1	981015	10:04	262	H	flm	N22W01	981018	19:28	981019	05:00	425	90.9	0.14	522	84.4
2	990707	19:31	547	PH	C1.1/SF	S26W69	990712	01:20					−0.35	367	89.3
3	991222	02:30	570	H	M1.8/2B	N10E30	991226	02:15	991226	08:24	411	101.9	−0.11	419	90.7[a]
4	000404	16:32	1188	H	C9.7/2F	N16W66	000406	16:27	000406	17:00	570	48.5	−0.31	587	55.0[a]
5	000714	10:54	1674	H	X5.7/3B	N22W07	000715	14:18	000715	19:00	990	32.1	−0.72	1038	30.8[a]
6	001025	08:26	770	H	C4.0	N06W61	001028	09:30	001028	23:18	375	86.9	−0.53	351	82.9[a]
7	010215	13:54	625	H	flm	N07E12	010220	00:54	010220	12:20	350	118.4	−0.56	295	95.5[a]
8	010228	14:50	313	PH	flm	S02W12	010303	11:30	010304	03:00	475	84.2	−0.06	515	76.5
9	010316	03:50	271	PH	flm	N11W09	010319	11:30	010319	23:18	420	91.5	0.58	636	92.9
10	010318	02:26	752	H	flm	S05W40	010320	13:30	010320	17:48	340	63.4	−0.30	485	69.8
11	010319	05:26	389	H	flm	S05W00	010322	14:00	010322	22:30	390	89.1	−0.01	441	92.1[a]
12	010329	10:26	942	H	X1.7/SF	N14W12	010331	01:14	010331	05:00	650	42.6	−0.13	782	47.6[a]
13	010402	22:06	2505	PH	X20	N19W72	010404	14:38	010404	20:54	740	46.8	−0.62	689	39.5[a]
14	010409	15:54	1192	H	M7.9/2B	S21W04	010411	14:12	010411	21:18	670	53.4	−0.49	600	50.1
15	010415	14:06	1199	PH	X14/2B	S20W85	010418	00:51	010418	05:20	520	63.2	−0.35	505	62.1
16	010426	12:30	1006	H	M7.8/2B	N17W31	010428	05:02	010429	01:48	640	61.3	−0.68	470	55.8[a]

(Continued on next page)

TABLE I
(Continued)

	CME				Flare		1-AU IP shock		1-AU ICME (MC/EJ)				IPS fitted		
No.	Date	h:m	V_{CME} (km s^{-1})	H/P	Class	Location	Date	h:m	Date	h:m	V_{ICME} (km s^{-1})	TT (h)	α	$V_{1\,AU}$ (km s^{-1})	TT (h)
17	010809	10;30	479	PH	flm	N05W05	010812	11:10	010813	08:00	400	93.5	−0.51	348	84.9[a]
18	010814	16:01	615	H	C2.3/SF	N16W36	010817	11:05	010817	20:00	550	76.0	−0.05	419	87.6[a]
19	010825	16:50	1433	H	X5.3/3B	S17E34	010827	19:40	010828	04:00	575	59.2	−0.37	585	54.4
20	010924	10:30	2402	H	X2.6/	S16E23	010925	20:18	010926	0100	600	38.5	−0.71	585	44.0[a]
21	010927	04:54	509	PH	C3.8/SF	S20W27	010929	09:25	010929	15:00	700	58.1	0.31	948	51.9
22	010928	08:54	846	H	M3.3/2N	N10E18	010930	19:15	011001	00:00	530	63.1	−0.23	599	59.2
23	011019	16:50	901	H	X1.6/2B	N15W29	011021	16:40	011022	01:00	660	56.2	−0.29	627	54.6
24	011022	15:06	1336	H	M6.7/2N	S21E18	011025	09:00	011025	18:00	430	74.9	−0.55	407	70.5
25	011025	15:26	1092	H	X1.3/2B	S16W21	011028	03:10	011028	11:00	460	67.6	−0.34	515	64.2
26	011104	16:35	1810	H	X1.0/3B	N06W18	011106	01:45	011106	06:00	700	37.4	−0.61	589	45.7[a]
27	011122	23:30	1437	H	M9.9	S14W36	011124	06:00	011124	15:48	730	40.3	−0.65	723	36.9
28	031104	19:54	2657	H	X28/3B	S19W83	031106	19:14	031107	00:00	570	52.1	−0.76	599	40.7[a]
29	031118	08:50	1660	H	M3.9/2N	N00E18	031120	07:28	031120	09:00	700	48.2	−0.15	742	49.4[a]
30	040725	14:54	1333	H	M1.1/1F	N08W33	040726	22:28	040727	03:00	1050	36.1	0.06	982	43.2[a]

Columns 2–5: white-light CME date, time (hh:mm), speed (km s^{-1}), type (halo/partial halo). Columns 6–7: flare class and location ('flm' indicates the filament eruption). Columns 8–9: IP shock arrival date and time (hh:mm) at 1 AU. Columns 10–13: ICME arrival date, time (hh:mm), speed (km s^{-1}) at 1 AU and transit time (h). Columns 14–16: speed–distance slope, α, speed (km s^{-1}) and transit time (h) at 1 AU predicted from the speed–distance profile.
[a]CME interacts with other CME(s).

3. Interplanetary Scintillation

The IPS observations reported in this study have been obtained from the ORT, operated by Radio Astronomy Centre, Tata Institute of Fundamental Research, India, at 327 MHz. Manoharan (2003, and references therein) has given a detail discussion on the IPS theory and Ooty observational and analysis procedures. In brief, the phenomenon of IP scintillation arises when radio waves from a distant compact source pass through the plasma density irregularities of the solar wind producing a random diffraction pattern on the ground and the motion of these irregularities at the speed of the solar wind converts this pattern into temporal intensity scintillations. The degree of scintillation is characterized by the scintillation index,

$$m = \frac{\text{rms of intensity fluctuations}}{\text{mean source intensity}},$$

which increases with decreasing distance (R) between the Sun and the line-of-sight to the radio source, until it reaches a maximum at $R \approx 40\,R_{\odot}$. In the weak-scintillation region (*i.e.*, at $R \geq 40\,R_{\odot}$), the intensity scintillation is linearly related to the electron-density fluctuations (Manoharan, 1993). The decline in scintillation at distances away from the transition point is caused by the fall of density (as well as density fluctuations turbulence) approximately as a function of inverse square of heliocentric distance. However, in the strong-scintillation region ($R < 40\,R_{\odot}$), the relationship between the scintillation and the density fluctuations is not straightforward and as the radio source approaches the Sun, the scintillation index decreases steeply, which is due to the smearing caused by the angular size of the radio source (Manoharan *et al.*, 1995).

Figure 2 shows the plot of scintillation index (m) observed over the years 1986–2004 as a function of heliocentric distance (R) for the well-known radio quasar

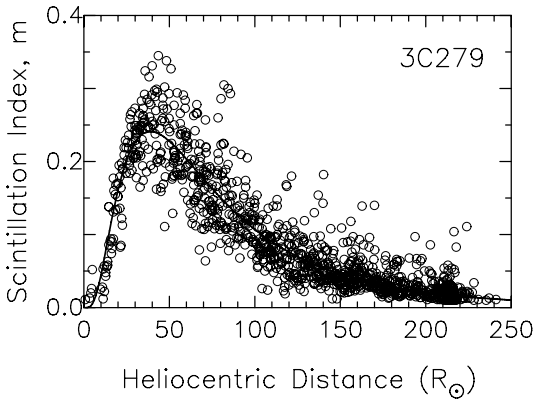

Figure 2. Scintillation indexes of the radio quasar 3C279 observed at 327 MHz, at different heliocentric distances. The plot has been made using measurements taken during the period 1986–2004. The average expected scintillation index is shown by the best fit *solid line*.

1253-055 (3C279), which has an angular diameter, $\Theta \approx 40$ marcsec. As discussed previously, the scintillation peaks around the heliocentric distance where the transition of weak to strong scattering occurs (*i.e.*, around 40 $R_\odot$). Manoharan (1993) has shown that the transition region can move toward or away from the Sun depending on the changes in the level of turbulence of large-scale density irregularities. At a given distance from the Sun, a large deviation above (or below) the mean curve seen in the scintillation indicates the high level of turbulence due to transients (or depletion of turbulence) in the solar wind. Furthermore, since the scintillation plot of the radio quasar 3C279 has been made using observations taken over several years, this plot would therefore include any systematic variations caused by the solar cycle changes.

3.1. Normalized scintillation index

The normalized scintillation index, generally denoted by g, is the ratio of the observed scintillation index of a radio source at a given distance from the Sun and its long-term baseline value of the scintillation index at the same distance, as given by,

$$g = \frac{\text{observed scintillation } (m(R))}{\text{average expected scintillation } (\langle m(R) \rangle)}.$$

In Figure 2, the average expected scintillation index, *i.e.*, the long-term baseline value, is shown by the best fit solid line. The normalized index, g, (and hence the rms of density fluctuations, δN; refer to equation of scintillation index, m) correlates strongly with the solar wind density (N) with a relationship $g = \sqrt{(N/9)}$ (Tappin, 1986; Rickett and Coles, 1991; Manoharan, 1993) and it can be used to assess the density-turbulence condition of the solar wind. For example, the value of g close to unity indicates the undisturbed condition of the solar wind, whereas $g > 1$ corresponds to the enhanced level of plasma density turbulence, and, $g < 1$ indicates the reduction of density in the solar wind. In the case of a moving CME, IPS measurements can easily detect the excess of turbulence produced by the compression of solar wind between the shock and the driving cloud, *i.e.*, the CME (*e.g.*, Manoharan, 1995; Manoharan *et al.*, 1995, 2000; Janardhan *et al.*, 1996; Tokumaru *et al.*, 2003).

3.2. Interplanetary scintillation images

At 327 MHz ($\lambda = 0.92$ m), the regular monitoring of IPS on a given radio source using a single-antenna system of good sensitivity, such as the ORT, can provide the speed and density turbulence of the solar wind at heliocentric distances $R \approx 20$–225 $R_\odot$ in the three-dimensional heliosphere (Manoharan and Ananthakrishnan, 1990; Tokumaru *et al.*, 1991; Manoharan *et al.*, 1995). Additionally, the importance of the IPS technique increases when the day-to-day monitoring of the heliosphere is made on a grid of large number of radio sources, whose lines of sight cut across different parts of the heliosphere. Although IPS

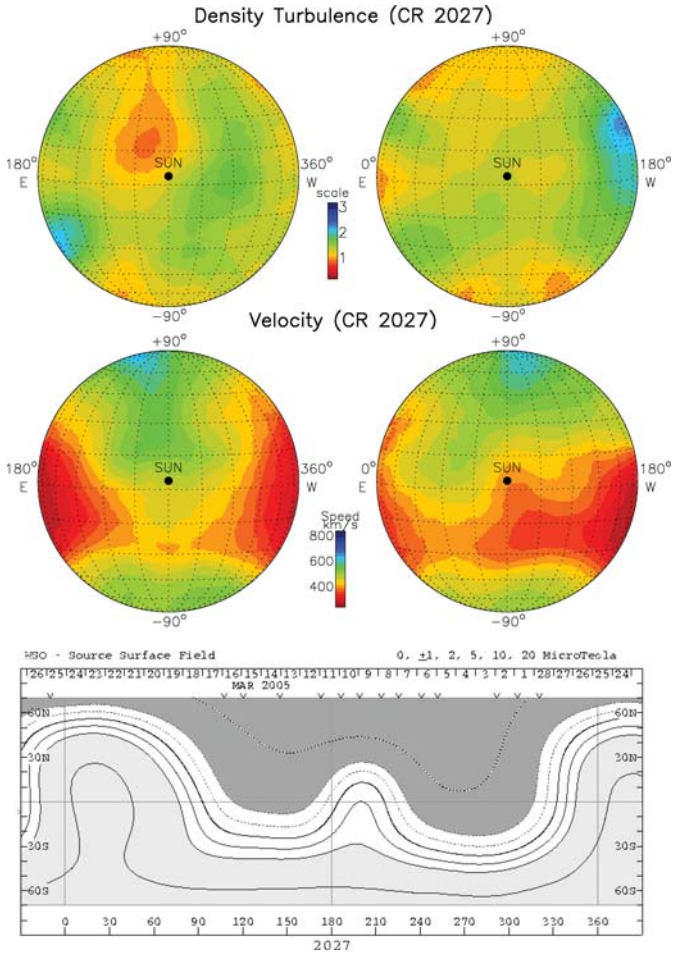

Figure 3. Two-dimensional images of density turbulence (*top panel*) and speed (*middle panel*) of the solar wind plasma for the Carrington Rotation 2027. In the *bottom panel*, for comparison, the solar source surface magnetic field observed at Wilcox Solar Observatory is also shown.

measurements are integrated along the path of the radio signal, the image processing of the normalized scintillation indexes (g-values) and the estimated speeds for the grid of sources provides the three-dimensional view of the ambient solar wind as well as the turbulent regions associated with the propagating disturbances in the IPS field of view. A tomographic analysis of the previous measurements will reveal the sharp boundary between the transient and background solar wind (*e.g.*, Kojima *et al.*, 1998). At Ooty, till the year 2002, the daily monitoring of the scintillation was made on about 300–400 radio sources and in the recent years, it has been increased to about 700 or more sources per day.

Figure 3 shows some samples of results obtained from the Ooty IPS measurements, namely, two-dimensional images of the solar wind density turbulence (top

panel) and speed (middle panel) traced backward/forward from the measurement point onto the heliosphere of radius $\sim$100 $R_\odot$. These images correspond to Carrington Rotation (CR) 2027. In the bottom panel of Figure 3, the computed synoptic map of the source surface magnetic field at 2.5 $R_\odot$ for the same rotation from the Wilcox Solar Observatory is shown. The comparison of images of density turbulence, speed, and source surface field reveals the correlation between the large structures of the solar wind parameters. However, a careful examination on finer scale would provide information on the source and acceleration of the solar wind (*e.g.*, Manoharan, Kojima, and Misawa, 1994).

4. Results and Discussion

4.1. 'SPEED–DISTANCE' PROFILES

An image produced from the IPS measurements made in an interval of time in a given day provides the status of the solar wind during that time in the observed field of view. Such snapshot images of the interplanetary medium made successively in time are equivalent to the white-light images and they are extremely useful to follow the three-dimensional evolution of the ambient solar wind and the transient plasma at large distances from the Sun, 50–250 $R_\odot$. Figure 4 shows scintillation images obtained from the Ooty measurements for (1) a full halo CME on July 14, 2000 (corresponding LASCO white-light images of this event are shown in Figure 1) at two time intervals, and (2) a partial halo CME on 2 April 2001 on four consecutive time intervals. These images indicate the presence of interplanetary CMEs and shocks as the CMEs propagated outward from the LASCO field of view.

In these 'PA–heliocentric distance' images, the north is at the top and east is to the left. The concentric circles are of radii, 50, 100, 150, 200 $R_\odot$. The red color code indicates the background (ambient) solar wind. In these images observing time increases from right (west of the Sun) to left (east of the Sun). For the Earth-directed halo CME on July 14, 2000, an east–west symmetry is expected on the scintillation images. But, the east–west positional shift with respect to the Sun, seen in the large enhanced scintillation region in the top-left image, is due to the time difference between the west and east measurements (*i.e.*, the CME is expanding with time). On 15 and 16 July IPS images, one may also notice the onset and propagation of another partial halo CME moving to the east, respectively, at $\sim$75 and $\sim$150 $R_\odot$. Thus, Ooty IPS measurements are highly sensitive to even less intense events (see Manoharan *et al.*, 2001). On the images corresponding to the partial halo on April 2, 2001, the CME onset in the IPS field of view is seen in the first images (see image on the left of the second row, 2 April, 21 UT to 3 April, 7 UT) at $\sim$50 $R_\odot$ along the south-west direction. The CME propagation can be observed in other later images.

In the same figure (bottom row), images obtained from IPS simulations for the idealistic halo and partial halo CMEs are also plotted for comparison at the bottom.

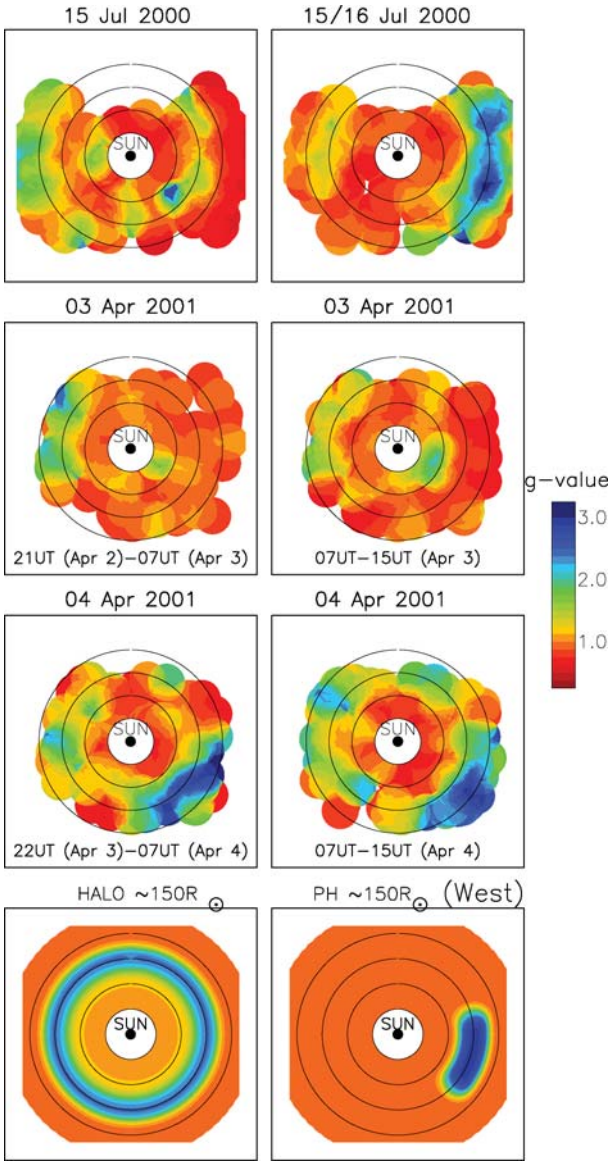

Figure 4. Ooty scintillation images of halo and partial halo CMEs observed on 14 July 2000 (2 images at the *top row*) and 2 April 2001 (4 images in the *middle*), respectively. The 2-April CME moving in the south-west direction is clearly seen on the IPS images. The enhancements associated with these CMEs are at different heliocentric distances (between ~50 and 225 $R_{\odot}$). The *concentric circles* are at radii 50, 100, 150, and 200 $R_{\odot}$. Simulated scintillation images of halo and partial halo (moving to the west) CMEs are shown for comparison at the *bottom row*. Since the IPS is sensitive to the solar wind flow perpendicular to the line of sight, on a grid of radio sources, the excessive scintillation caused by a halo CME would, in principle, appear as a ring-shaped pattern centered around the Sun.

The three-dimensional MHD simulations have also produced similar results (Tappin *et al.*, 1988). On the observed IPS snapshot images, the CME onset time and distance are determined and the height–time plot is prepared as discussed later.

The speed profile of each CME between the Sun and 1 AU is determined by fitting a second-order polynomial to the height–time plot obtained by combining LASCO and IPS measurements. But, since the height–time measurements are made in the sky plane, the speed derived from such a plot represents the lower limit due to the projection effect, which is maximum for a disk-centered halo event and it decreases as the location of the CME approaches the solar limb. However, the present analysis of speeds of partial halo CMEs originating close to the solar limb has shown that the rate of expansion of the CME in the lateral direction is nearly same as its speed along the radial propagation path. This is consistent with the near-Sun region results (*e.g.*, Dal Lago, Schwenn, and Gonzalez, 2003). Furthermore, a sufficiently large partial halo CME would appear as a full halo when viewed along its propagation path. Therefore, in the present study, the estimated speed of a halo CME in the sky plane is considered as the propagation speed of the CME without taking projection effects into account. Figure 5 shows typical examples of speed–distance profiles derived by combining the LASCO and IPS data points for (1) an accelerating CME between Sun and Earth, (2) a constant speed event, and, (3) some decelerating cases. The data points at $R \leq 30\,R_\odot$ and $R \geq 80\,R_\odot$ are from LASCO and IPS measurements, respectively. The radial profiles of most of the CMEs show that they tend to attain the speed of the ambient flow at 1 AU or larger distances.

4.2. Initial speed and speed profile, $V_{\mathrm{CME}}(R)$

It is evident from the speed–distance profiles that at heliocentric distance ranges, (1) Sun to 50 $R_\odot$ and (2) in the range 100–200 $R_\odot$, the radial dependence of the speed of the CME, $V_{\mathrm{CME}}(R)$, can be represented by power-law forms, $V_{\mathrm{CME}}(R) \sim R^{-\beta}$ and $V_{\mathrm{CME}}(R) \sim R^{-\alpha}$, respectively (refer to Figure 5). The transition from the flat portion to the steeper part occurs at about 60–80 $R_\odot$. The values of α and β derived for all the events respectively vary in the range, $-0.76 \leq \alpha \leq 0.58$ and $-0.3 \leq \beta \leq 0.06$. The radial slope, index α, is listed in Table I.

At the large-distance part, at $R \geq 80\,R_\odot$, the crucial data points have been provided by the IPS measurements. In this region, when a net effective acceleration is observed, the radial dependence of the speed of the CME is steeper than that of LASCO field of view. However, a couple of CMEs have been observed with constant speed for the entire Sun–Earth distance and for these cases, the power-law indexes, α and β, lie close to the null value. The index β does not show a significant dependence on the initial speed of the CME. While on the contrary, the index α shows a systematic change with the CME speed and it provides the state of effective acceleration experienced by the CME before reaching the Earth's orbit.

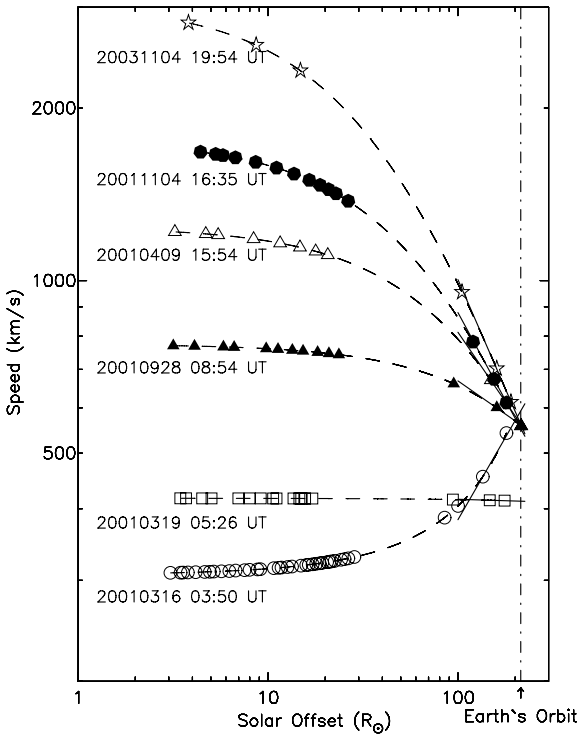

Figure 5. Representative speed–distance, $V(R)$, profiles plotted on log–log scale. Average initial speed of the CME increases from bottom ($\sim$300 km s^{-1}) to top ($\sim$2500 km s^{-1}). The date and the start time of each CME are shown. These profiles converge toward the ambient solar wind speed at the Earth's orbit. The data points at $R \leq 30\ R_{\odot}$ and $R \geq 80\ R_{\odot}$ are from LASCO and IPS measurements, respectively. The *straight-line* fit to the data points at $R \geq 100\ R_{\odot}$ gives the slope, α, according to $V \sim R^{-\alpha}$ (refer to Section 4.2). The *vertical line* indicates the Earth's orbit ($R \approx 215\ R_{\odot}$).

Figure 6 shows the index α plotted as a function of the initial speed of the CME. The horizontal dashed line at $\alpha = 0$ indicates a null acceleration line at distances $R \geq 100\ R_{\odot}$. A number of events are believed to include complex situation wherein the CME interacts with a preceding one and these events are boxed with the square symbol in Figure 6 and in later figures. The events originating at longitude or latitude greater than 35° are enclosed in circles. The data points lying above the null-acceleration line (*i.e.*, $\alpha < 0$) go through a moderate to severe deceleration. It is important to note that 26 out of 30 events have shown deceleration in the IPS distance range. The steepening of the speed profile increases with the initial speed of the CME. The solid curve is the second-order least-square fit to the data points and it relates the index α with the initial speed, $V_{\rm CME}$, at $R \geq 100\ R_{\odot}$, as given by,

$$\alpha = 0.2\text{–}6.4 \times 10^{-4} V_{\rm CME} + 1.1 \times 10^{-7} V_{\rm CME}^2. \quad (1)$$

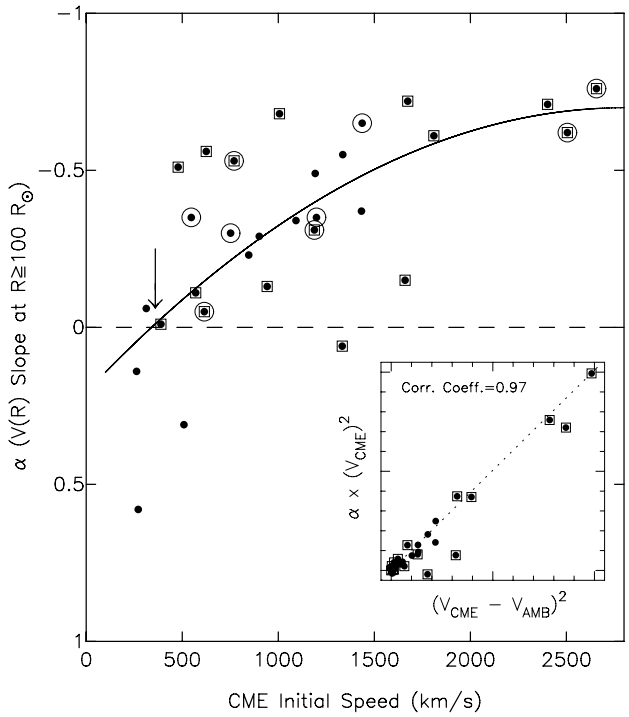

Figure 6. Slope, α, of speed–distance profile ($V_{\rm CME}(R)$) (at distances $R \geq 100\,R_{\odot}$) plotted as a function of initial speed of the CME, $V_{\rm CME}$. The data points enclosed with *square symbols* represent CMEs that interact with preceding CME(s) and CMEs originating at longitude/latitude $>35^{\circ}$ are enclosed in *circles*. The radial profile becomes steeper with the initial speed of the CME. The best-fit curve is shown by a *solid line*. The *dashed line* indicates the 'zero' acceleration line. The *arrow* indicates the threshold speed, $\sim$380 km s^{-1}, which determines the effective acceleration effected on the moving CME by the solar wind interaction. The data points showing large deviation from the best-fit mean curve are due to the interaction between CMEs and/or with the ambient solar wind. The *inset* shows the correlation plot between $\alpha \times V_{\rm CME}^2$ and $(V_{\rm CME}{-}V_{\rm AMB})^2$, where $V_{\rm AMB}$ is the speed of the ambient solar wind. This plot reveals the crucial part played by the interaction of the CME with the background solar wind.

In Figure 6, the data points showing large deviation from the mean curve (Equation (1)) have mainly been affected by interactions with CME(s) and/or with the background solar wind (*i.e.*, events having large effective acceleration due to the background solar wind). It is in good agreement with the results on influence of interactions obtained by Manoharan *et al.* (2004).

4.3. Threshold initial speed and solar wind interaction

In Figure 6, the best-fit curve cuts the 'zero' acceleration line at about 380 km s^{-1}, which is nearly same as the speed of the ambient flow and it is the threshold speed,

which decides an event's acceleration or deceleration. In addition, the fitted curve shows the average propagation characteristics of CMEs, under the undisturbed condition of the solar wind, for a range of initial speeds. However, the large deviations from the mean curve to the 'upward' or 'downward' directions are likely due to the 'deceleration' (*i.e.*, hindrance to propagation) or 'acceleration' (*i.e.*, assistance to propagation), respectively, caused by the CME–CME interaction and the background solar wind. The speed profiles (refer to Figure 5) converging to the speed of the ambient flow at the Earth's orbit confirm the effectiveness of the drag force imposed on the CME by the interaction with the ambient wind.

In Figure 6, only four events show acceleration in the IPS distance range (*i.e.*, $\alpha > 0$). In particular, a CME event with a high initial speed ($V_{\mathrm{CME}} = 1333\,\mathrm{km\,s^{-1}}$, refer to number 30 in Table I) shows the acceleration, although marginal (*i.e.*, $\alpha = 0.06$), in the IPS field of view. This event was clearly associated with a solar active region, which produced multiple CMEs. Therefore, it is likely that the interactions between CMEs and solar wind have modified and resulted in a disturbed interplanetary medium, which tends to aid the propagation of the CME. Other three events (refer to Table I, numbers 1, 9, and 21) started with speeds of 262, 271, and 509 $\mathrm{km\,s^{-1}}$, respectively. Since the speeds of two events (numbers 1 and 9) were lower than the typical background solar wind speed of $\sim$380 $\mathrm{km\,s^{-1}}$ (refer to Figure 6), they naturally would have been carried and accelerated by the solar wind flow. The third one (number 21), although with a linear speed of 509 $\mathrm{km\,s^{-1}}$, went through a considerable acceleration in the LASCO field of view and attained a high speed of $\sim$1600 $\mathrm{km\,s^{-1}}$ at $R \approx 28\,R_{\odot}$. This event arrived at 1 AU in $\sim$58 h with a speed of $\sim$700 $\mathrm{km\,s^{-1}}$. These results suggest that the event has gone through a considerable acceleration, aided by the energy gained at the time of CME onset and stored within the CME.

The findings mentioned previously confirm that the major force acting on a moving CME is caused by the interaction of the CME with the structures of the solar wind and results are in good agreement with the earlier studies (*e.g.*, Lindsay *et al.*, 1999; Gopalswamy *et al.*, 2000; Manoharan *et al.*, 2004). It is however essential to quantify the interacting force. In the fluid dynamics, the interaction (or 'drag force') between a moving cloud and the gaseous medium is governed by the square of the relative speed between them. For example, the aerodynamic drag force acting on a CME has been modeled by numerical simulations (*e.g.*, Cargill *et al.*, 1996; Vandas *et al.*, 1996; Cargill, 2004). In Figure 6(b), the index α times the square of the initial speed of the CME ($\alpha \times V_{\mathrm{CME}}^2$) is plotted against the square of the relative speed, $(V_{\mathrm{CME}}-V_{\mathrm{AMB}})^2$, where V_{AMB} is the speed of the ambient solar wind. The average ambient speed, $V_{\mathrm{AMB}} \approx 400\,\mathrm{km\,s^{-1}}$, has been obtained from the daily scintillation measurements. This plot shows a high degree of linear correlation, coefficient $\sim$97%, which indicates that the index α associated with a CME represents the amount of energy utilized/gained ($\sim V_{\mathrm{CME}}^2$) in the background flow. It is important to note that in a realistic situation, the speed of the ambient solar wind, V_{AMB}, should be a function of heliocentric distance to reflect the actual

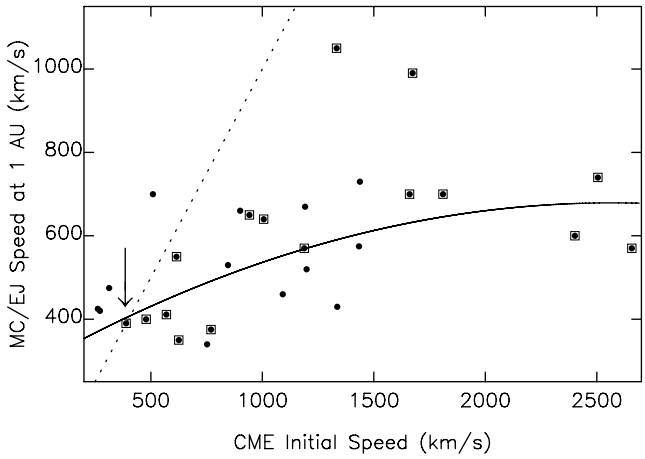

Figure 7. Initial speed of the CME plotted as a function of observed MC/EJ speed at 1 AU. The *dotted line* is the 'zero' acceleration line. The *solid curve* is the best fit to the data points. The *arrow* indicates the initial threshold speed, $\sim$385 km s^{-1} (refer to Figure 5), and events with speed lower than this will experience an acceleration and those with higher speeds will show deceleration. The data points enclosed with *square symbols* represent CMEs that interact with preceding CME(s).

solar wind conditions along the path of the CME (*e.g.*, Gosling and Riley, 1996; Gosling *et al.*, 1998).

4.4. Speed and arrival time at 1 AU

In Figure 7, the speed of the CME at 1 AU and corresponding initial speed are plotted. The 'zero' effective acceleration is indicated by the dotted line, on which the initial speed of the CME equals the final speed of MC/EJ at the Earth's orbit. It is clear that except for four cases, all the CMEs went through a moderate to severe deceleration before the arrival at 1 AU. However, out of these four cases, three events have also shown $\alpha > 0$ (refer to Table I, numbers 1, 9, and 21) and as discussed in Section 4.3, they have been likely accelerated before the arrival at 1 AU. The fourth event (Table I, number 8) was observed with an initial speed of 313 km s^{-1} and a marginal acceleration in the LASCO field of view. The index α ($= -0.06$) at the IPS region indicates that this event has traveled with not much of speed variation.

A least-square fit to the data points in Figure 7 provides an average relationship between the initial speed (V_{CME}) of the CME and the final speed (*i.e.*, speed of MC/EJ) at 1 AU, as given by,

$$V_{\mathrm{MC/EJ}} = 300 + 3 \times 10^{-1} V_{\mathrm{CME}} - 6 \times 10^{-5} V_{\mathrm{CME}}^2. \quad (2)$$

This best-fit curve crosses the 'zero' acceleration line at a speed of $\sim$ 385 km s^{-1}, which is same as the threshold speed obtained from Figure 6(a). As discussed in

Section 4.3, this speed determines the effective acceleration imposed on a CME through interaction.

For each CME, the overall fit to the LASCO and IPS measurements (*e.g.*, refer to radial profiles shown in Figure 5) has also been used to estimate the expected travel time and speed of the MC/EJ at 1 AU. These estimates are also listed in Table I. The comparison between the observed and predicted travel times shows a good correlation of ∼96%, which confirms that the fitted profile of speed depicts the actual path of the CME. Before arriving at 1 AU, however, a CME is likely to encounter large-scale structures of varying physical properties to assist or hinder the propagation. It is partly reflected on the correlation between the observed and estimated speeds of MC/EJ at 1 AU (see Table I). A rms variation of $\sim 70\,\mathrm{km\,s^{-1}}$ is found between these speeds. The average observed speed at 1 AU is $\langle V_{\mathrm{MC/EJ(obsd)}} \rangle = 573\,\mathrm{km\,s^{-1}}$ and the average predicted speed is $\langle V_{\mathrm{MC/EJ(pred)}} \rangle = 541\,\mathrm{km\,s^{-1}}$. The radial profile of speed of a CME thus obtained combining the LASCO and IPS images yields a factual view, which is nearly close to the actual speed variation, of the propagation of the CME in the inner heliosphere.

4.5. CME'S INTERNAL ENERGY

Figure 8 displays the observed travel time of the CME to 1 AU as a function of its initial speed, V_{CME}. It is evident that for a given initial speed, a range of travel times is observed, suggesting that each CME is going through different kind of interaction and/or acceleration. This result further suggests that the large-scale structures of the solar wind encountered by the CME tend to shape the radial-speed profile. The travel times predicted from the speed profiles obtained by combining

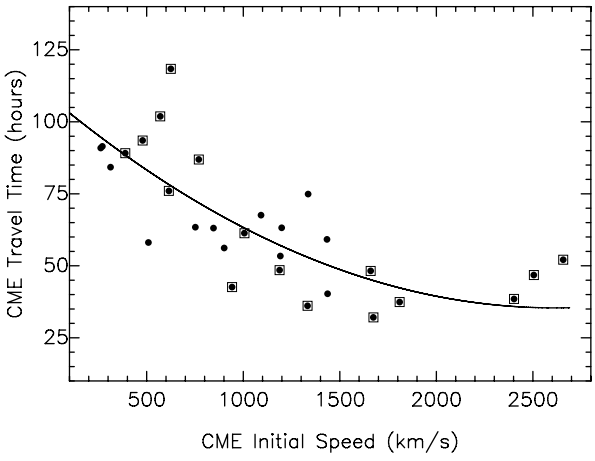

Figure 8. Initial speed of the CME plotted as a function of observed travel time to 1 AU. The *solid curve* is best fit to the data points. The data points enclosed with *square symbols* represent CMEs that interact with preceding CME(s).

the LASCO and IPS data (see Table I) show less scatter than seen in Figure 8. It thus demonstrates that the realistic radial profiles are obtained from the present study and results also reiterate the essential need to measure the propagation of the CME at multiple distances before it hits at 1 AU. The least-square fit to the data points, drawn by the solid line in the figure, shows a steady decrease in travel time as the initial speed increases. It provides the typical travel time for a given initial speed, as given by,

$$T_{\mathrm{CME}} = 108.6 - 0.5 \times 10^{-1} V_{\mathrm{CME}} + 1.1 \times 10^{-5} V_{\mathrm{CME}}^2. \quad (3)$$

An interesting point to be noted in the previous Equation is that a CME moving with a speed of the ambient solar wind (*e.g.*, $\sim$400 km s^{-1}) would hit the Earth's orbit at $\sim$90 h. However, the typical solar wind with the same speed takes about 103 h to cross the Sun–Earth distance. The 13-h difference in the aforementioned transit times suggests that the propagation of the CME is supported by the energy stored within itself. In other words, the transit time derived from the previous equation includes the energy stored in the CME and/or interaction to impose an effective acceleration on the propagation. Therefore, many questions related to the evolution of a CME in the interplanetary medium are also closely connected to the magnetic configuration at the origin of the CME on the solar surface. For example, most of the CMEs expand as they move outward in the solar wind and some of them travel faster than the highest speed solar wind. The expansion/acceleration is probably to be associated with the outward pressure exerted by the CME cloud. The interaction of the CME with the background solar wind, although complex, plays a key role in the overall physics of the expansion. Therefore, the next natural question is that how long or how far the expansion of the CME (and the resulting acceleration) can support the propagation. Manoharan *et al.* (2000, 2001, 2002) have shown that at distance, $R < 80\,R_{\odot}$, the acceleration is dominated by the expansion of the CME and at larger distances, the interaction with the ambient solar wind dominates. In Figure 5, the change in slope, *i.e.*, β to α transition, takes place at $\sim$60–80 $R_{\odot}$ and it suggests a change from the CME expansion dominated region to the solar wind interaction influenced space. The relationship between the index, α, and initial speed of the CME, V_{CME} (Equation (1)), is mostly interaction dominated and the relationship (Equation (3)) between the travel time and the initial speed of the CME confirms the partial support provided by the magnetic energy in the propagation to 1 AU. However, for the high-speed CMEs (*e.g.*, $V_{\mathrm{CME}} \geq 2000$ km s^{-1}), the travel time is mostly controlled by the interaction of the CME with the solar wind.

5. Summary

In this study, the analysis of radial evolution of 30 large angular width CMEs has been carried out for the Sun to 1 AU distance range by combining the white-light and

IPS images. These CMEs cover a wide range of initial speeds, ∼260–2600 km s^{-1} and include categories of constant speed, accelerating, and decelerating CMEs in the Sun–Earth distance range. The results are as follows:

– The present analysis emphasizes the importance of the multi-point three-dimensional measurements of both CMEs and surrounding inhomogeneous solar wind to understand the complex evolution of CMEs in the interplanetary medium.
– It is broadly known that the CME having initial speed less than the ambient solar wind speed is accelerated by the surrounding solar wind and on the contrary, the high-speed CME is decelerated (*e.g.*, Vandas *et al.*, 1996; Lindsay *et al.*, 1999; Gopalswamy *et al.*, 2000; Manoharan *et al.*, 2004) and results of the present study are in good agreement with these earlier findings (refer to Figures 5 and 6).
– Many questions related to the evolution of CME in the interplanetary space are closely linked to the origin of the CME on the Sun. In other words, it is important to understand the dominant role played by the CME expansion over that of the interaction effected by the surrounding solar wind. The radial profile of the speed at distances $R \leq 50\ R_\odot$ ($V \sim R^{-\beta}$) is nearly flat and shows no significant dependence on the initial speed of the CME. It suggests that the CME expansion is stronger than the drag force and it likely ceases at about 60–90 $R_\odot$ where the transition takes place between indexes β and α.
– The radial speed of the CME tends to attain the speed of the ambient solar wind at 1 AU or further out of the Earth's orbit. The speed profile between the Sun and 1 AU and the arrival time of the CME at 1 AU reveal the combined influence of the CME expansion and the interaction at different regions of the inner heliosphere. But, the high-speed CME's radial index α at large distances, $R \geq 80\ R_\odot$, is steep and shows systematic change with the initial speed of the CME. The results are consistent with the individual event studies as well as the numerical simulations (*e.g.*, Smith and Dryer, 1990; Manoharan *et al.*, 2000, 2001; Gonzalez-Esparza *et al.*, 2003; Manoharan, 2003). Therefore, the radial-speed index, α, shows the effect of the drag force, applied by the surrounding solar wind, which tends to equalize the speed of the CME to that of the local solar wind speed (refer to Figure 5).
– The relationship shown in Figure 6 between the speed-profile index, α, and the relative speed (or the initial speed) of the CME depicts the evolution of the CME in the undisturbed steady solar wind condition. But, for several cases, it may be far from the realistic condition. The scatter seen in the plot confirms the heterogeneous structure of the solar wind. The cases decelerating more than the average curve have likely been more dragged and/or launched with considerably less internal energy. On the other hand, the events accelerating more than the average curve should possess large amount of expansion (or magnetic) energy to aid the propagation. The flat and/or no significant dependence of the index β

with the initial speed suggests that the eruption speed may not be directly linked to the internal energy of the CME.

Thus, each CME has a unique evolution trajectory and to predict the CME arrival at 1 AU, multi-point measurements are essential. In summary, the outward pressure exerted by the CME cloud tries to overcome the dynamic interaction with the solar wind and it supports the propagation up to a certain distance, which is less than 100 $R_{\odot}$. At larger distances, the crucial measurements provided by the IPS show that the interaction of the CME with the surrounding solar wind shapes the radial evolution of the CME. Measurements from the LASCO, the IPS on a large number of source, and the proposed STEREO mission combined together will provide a complete picture of the three-dimensional view of the CME propagation between the Sun and Earth.

Acknowledgements

The author thanks the observing and engineering staff of Radio Astronomy Centre for help in making the IPS observations. It is a great pleasure to thank N. Gopalswamy for many useful discussions. SOHO is a project of international cooperation between ESA and NASA. The author would like to thank for the excellent LASCO-CME Catalog, which includes supportive data. This CME catalog is generated and maintained by Center for Solar Physics and Space Weather, Catholic University of America, in cooperation with NASA and Naval Research Laboratory. The author acknowledges the teams of ACE/SWEPAM, ACE/MAG, WIND/MFI, and WIND/SWE for making the solar wind and magnetic field data available on the web and Wilcox Solar Observatory for the synoptic chart. The author thanks the referee for useful suggestions. The author also thanks N. Mariyappa for assistance in data reduction.

References

Anzer, U.: 1980, in M. Dryer and E. Tandberg-Hanssen (eds.), *Proc. IAU Symp.* **91**, 263.
Brueckner, G.E., Howard, R.A., Koomen, M.J., Korendyke, C.M., Michels, D.J., Moses, J.D., *et al.*: 1995, *Solar Phys.* **162**, 357.
Cane, H.V. and Reames, D.V.: 1988, *Astron. Phys. J.* **325**, 895.
Cane, H.V. and Richardson, I.G.: 2003, *J. Geophys. Res.* **108**, 1156.
Cane, H.V., Sheeley Jr., N.R., and Howard, R.A.: 1987, *J. Geophys. Res.* **92**, 9867.
Cargill, P.J.: 2004, *Solar Phys.* **221**, 135.
Cargill, P.J., Chen., J., Spicer, D.S., and Zalesak, S.T.: 1996, *J. Geophys. Res.* **101**, 4855.
Dal Lago, A., Schwenn, R., and Gonzalez, W.D.: 2003, *Adv. Space Res.* **32**, 2637.
Dryer, M.: 1974, *Space Sci. Rev.* **15**, 403.
Dryer, M.: 1994, *Space Sci. Rev.* **67**, 363.

Dryer, M., Eviatar, A., Frohlich, A., Jacobs, A., Joseph, J.H., and Weber, E.J.: 1974, in G. Newkirk Jr. (ed.), *Coronal Disturbances, Proc. IAU Symp.* **57**, 377.
Gapper, G.R., Hewish, A., Purvis, A., and Duffett-Smith, P.J.: 1982, *Nature* **296**, 633.
Gary, D.E., Dulk, G.A., House, L., Illing, R., Sawyer, C., Wagner, W.J., McLean, D.J., and Hildner, E.: 1984, *Astron. Astrophys.* **134**, 222.
Gonzalez-Esparza, J.A., Lara, A., Perez-Tijerina, E., Santillan, A., and Gopalswamy, N.: 2003, *J. Geophys. Res.* **108**, SSH 9-1.
Gopalswamy, N., Kaiser, M.L., Lepping, R.P., Kahler, S.W., Ogilvie, K., Berdichevsky, D., Kondo, T., Isobe, T., and Akioka, M.: 1998, *J. Geophys. Res.* **103**, 307.
Gopalswamy, N., Lara, A., Lepping, R.P., Kaiser, M.L., Berdichevsky, D., and St. Cyr, O.C.: 2000, *J. Geophys. Res.* **27**, 145.
Gopalswamy, N., Lara, A., Yashiro, S., Kaiser, M.L., and Howard, R.A.: 2001, *J. Geophys. Res.* **106**, 29207.
Gopalswamy, N., Yashiro, S., Kaiser, M.L., Howard, R.A., and Bougeret, J.-L.: 2002, *Geophys. Res. Lett.* **29**, 106.
Gopalswamy, N., Aguilar-Rodriguez, E., Yashiro, S., Nunes, S., Kaiser, M.L., and Howard, R.A.: 2005, *J. Geophys. Res.* **110**, 12S07, doi: 10.1029/2005JA011158.
Gosling, J.T.: 1990, in C.T. Russell, *et al*. (eds.), *AGU Monograph* **58**, 343.
Gosling, J.T. and Riley, P.: 1996, *Geophys. Res. Lett.* **23**, 2867.
Gosling, J.T., McComas, D.J., Phillips, J.L., and Bame, S.J.: 1991, *J. Geophys. Res.* **96**, 7831.
Gosling, J.T., Riley, P., McComas, D.J., and Pizzo, V.J.: 1998, *J. Geophys. Res.* **103**, 1941.
Han, S.M., Wu., S.T., and Dryer, M.: 1988, *Comp. Fluids* **16**, 81.
Hewish, A., Tappin, S.J., and Gapper, G.R.: 1985, *Nature* **314**, 137.
Hildner, E.: 1977, in M.A. Shea, *et al*. (eds.), *Proceedings of the L.D. De Feiter Memorial Symposium*, p. 3.
Janardhan, P., Balasubramanian, V., Ananthakrishnan, S., Dryer, M., Bhatnagar, A., and McIntosh, P.S.: 1996, *Solar Phys.* **166**, 379.
Kojima, M., Tokumaru, M., Watanabe, H., Yokobe, A., Asai, K., Jackson, B.V., and Hick, P.L.: 1998, *J. Geophys. Res.* **103**, 1981.
Lepping, R.P., Burlaga, L.F., Szabo, A., Ogilvie, K.W., Mish, W.H., Vassiliadis, D., *et al*.: 1997, *J. Geophys. Res.* **102**, 14049.
Lindsay, G.M., Luhmann, J.G., Russell, C.T., and Gosling, J.T.: 1999, *J. Geophys. Res.* **104**, 12515.
Lyubimov, G.P.: 1968, *Astron. Tsirk.* **488**, 4.
MacQueen, R.M.: 1980, *Philos. Trans. R. Soc. Lond.* **297**, 605.
Manoharan, P.K.: 1993, *Solar Phys.* **148**, 153.
Manoharan, P.K.: 1995, *Bull. Astron. Soc. India* **23**, 399.
Manoharan, P.K.: 2003, in H.M. Antia, *et al*. (eds.), *Lectures on Solar Physics*, Springer-Verlag, Heidelberg, Vol. 619, p. 299.
Manoharan, P.K. and Ananthakrishnan, S.: 1990, *Month. Not. R. Astron. Soc.* **244**, 691.
Manoharan, P.K., Kojima, M., and Misawa, H.: 1994, *J. Geophys. Res.* **99**, 23411.
Manoharan, P.K., Ananthakrishnan, S., Dryer, M., Detman, T.R., Leinbach, H., Kojima, M., Watanabe, T., and Kahn, J.: 1995, *Solar Phys.* **156**, 377.
Manoharan, P.K., Kojima, M., Gopalswamy, N., Kondo, T., and Smith, Z.: 2000, *Astrophys. J.* **530**, 1061.
Manoharan, P.K., Tokumaru, M., Pick, M., Subramanian, P., Ipavich, F.M., Schenk, K., Kaiser, M.L., Lepping, R.P., and Vourlidas, A.: 2001, *Astrophys. J.* **559**, 1180.
Manoharan, P.K., Pick, M., and LASCO Consortium.: 2002, in A.P. Rao, *et al*. (eds.), *The Universe at Low Radio Frequencies, Proc. IAU Symp.* **199**, 426.
Manoharan, P.K., Gopalswamy, N., Yashiro, S., Lara, A., Michalek, G., and Howard, R.A.: 2004, *J. Geophys. Res.* **109**, 6109.

Neugebauer, M. and Goldstein, R.: 1997, in N. Crooker, *et al*. (eds.), *Coronal Mass Ejection, AGU Monograph* **99**, 245.
Odstrcil, D.: 2003, *Adv. Space Res.* **32**, 497.
Pinter, S.: 1973, *Nature Phys. Sci.* **243**, 96.
Purvis, A., Tappin, S.J., Rees, W.G., Hewish, A., and Duffett-Smith, P.J.: 1987, *Month. Not. R. Astron. Soc.* **229**, 589.
Reames, D.V.: 1996, in R. Ramaty, *et al*. (eds.), *AIP Conference Proceedings of the American Institue of Physics*, New York, Vol. 374, p. 35.
Rickett, B.J. and Coles, W.A.: 1991, *J. Geophys. Res.* **96**, 1717.
Selvanayagam, A.J., Praveenkumar, A., Nandagopal, D., and Velusamy, T.: 1993, *IETE Tech. Rev.* **10**, 333.
Sheeley Jr., N.R., Howard, R.A., Koomen, M.J., Michels, D.J., Schwenn, R., Muhlhauser, K.H., and Rosenbauer, H.: 1985, *J. Geophys. Res.* **90**, 163.
Smith, Z. and Dryer, M.: 1990, *Solar Phys.* **129**, 387.
Srivastava, N. and Venkatakrishnan, P.: 2002, *Geophys. Res. Lett.* **29**, 1287.
Stewart, R.T.: 1980, in M. Dryer and E. Tandberg-Hanssen (eds.), *Proc. IAU Symp.* **91**, 333.
Sun, W., Deehr, C.S., Fry, C.D., Dryer, M., Smith, Z., and Akasofu, S.-I.: 2003, *Geophys. Res. Lett.* **30**, 2044.
Swarup, G., Sarma, N.V.G., Joshi, M.N., Kapahi, V.K., Bagri, D.S., Damle, S.H., Ananthakrishnan, S., Balasubramanian, V., Bhave, S.S., and Sinha, R.P.: 1971, *Nature Phys. Sci.* **230**, 185.
Tappin, S.J.: 1986, *Planet. Space Sci.* **34**, 93.
Tappin, S.J., Dryer, M., Han, S.M., and Wu, S.T.: 1988, *Planet. Space Sci.* **36**, 1155.
Tokumaru, M., Mori, H., Tanaka, T., Kondo, T., Takaba, H., and Koyama, Y.: 1991, *J. Geomag. Geoelectr.* **43**, 619.
Tokumaru, M., Kojima, M., Fujiki, K., Yamashita, M., and Yokobe, A.: 2003, *J. Geophys. Res.* **108**, 1220.
Vandas, M., Fischer, S., Dryer, M., Smith, Z., and Detman, T.: 1996, *J. Geophys. Res.* **101**, 15645.
Vlasov, V.I.: 1992, in S. Fischer and M. Vandas (eds.), *Proceedings of the First SOLTIP Symposium*, Czechoslovak Academy of Science, Liblice, Vol. 1, p. 273.
Vilmer, N., Pick, M., Schwenn, R., Ballatore, P., and Villain, J.P.: 2003, *Ann. Geophys.* **21**, 847.
Webb, D.F., Cliver, E.W., Crooker, N.U., St. Cyr, O.C., and Thompson, B.J.: 2000, *J. Geophys. Res.* **105**, 7491.
Woo, R., Armstrong, J.W., Sheeley Jr., N.R., Howard, R.A., Koomen, M.J., Michels, D.J. and Schwenn, R.: 1985, *J. Geophys. Res.* **90**, 154.
Woo, R., Armstrong, J.W., Bird, M.K., and Patzold, M.: 1995, *Geophys. Res. Lett.* **22**, 329.
Yashiro, S., Gopalswamy, N., Michalek, G., St. Cyr, O.C., Plunkett, S.P., Rich, N.B., and Howard, R.A.: 2004, *J. Geophys. Res.* **109**, 7105.
Zhang, J., Dere, K.P., Howard, R.A., and Bothmer, V.: 2003, *Astrophys. J.* **582**, 520.